Metastability of Liquid Water Freezing into Ice VII under Dynamic Compression

M. C. Marshall, M. Millot, D. E. Fratanduono, D. M. Sterbentz, P. C. Myint, J. L. Belof, Y.-J. Kim, F. Coppari, S. J. Ali, J. H. Eggert, R. F. Smith, and J. M. McNaney

Phys. Rev. Lett. **127**, 135701 — Published 23 September 2021

DOI: 10.1103/PhysRevLett.127.135701

Metastability of liquid water freezing into ice VII under dynamic compression

M. C. Marshall,[1,2,*] M. Millot,[1] D. E. Fratanduono,[1] D. M. Sterbentz,[1,3] P. C. Myint,[1] J. L. Belof,[1] Y.-J. Kim,[1] F. Coppari,[1] S. J. Ali,[1] J. H. Eggert,[1] R. F. Smith,[1] and J. M. McNaney[1]

[1] *Lawrence Livermore National Laboratory, Livermore, California 94550, USA*
[2] *Laboratory for Laser Energetics, Rochester, New York 14623, USA*
[3] *Department of Mechanical and Aerospace Engineering, University of California, Davis, California 95616 USA*

(Dated: July 29, 2021)

The ubiquitous nature and unusual properties of water have motivated many studies on its metastability under temperature- or pressure-induced phase transformations. Here, nanosecond compression by a high-power laser is used to create the nonequilibrium conditions where liquid water persists well into the stable region of ice VII. Through our experiments, as well as a complementary theoretical/computational analysis based on classical nucleation theory, we report that the metastability limit of liquid water under nearly isentropic compression from ambient conditions is at least 8 GPa, higher than the 7 GPa previously reported for lower loading rates.

Water at extreme conditions has attracted recent attention owing to its complex phase diagram, including superionic ice phases having exotic properties that exist at high pressures and densities [1, 2]. To date, 20 unique crystalline ice phases have been found naturally on Earth or in the laboratory [2–8]. The structural, electronic, and thermal properties of these high-pressure ices have implications for our understanding of celestial bodies with high concentrations of water [3, 9]. Ice VII, the solid phase of interest in this work, is the stable polymorph of water at room temperature and at pressures exceeding ∼2 GPa (Fig. 1) [10]. Recently, ice VII was found naturally on Earth for the first time as inclusions in diamonds sourced deep within the mantle [11]. It may exist inside Jupiter's icy moons and in water worlds beyond our solar system [3].

Metastability of liquid water at conditions where solid ice is the stable phase is an active area of research, despite the difficulty of creating transient metastable samples and probing them before solidification. There are studies examining the liquid–liquid phase transition and searching for the liquid–liquid critical point in supercooled liquid water that may help explain water's anomalous properties [14–20]. As an alternate approach to supercooling, one can rapidly compress liquid water to pressures exceeding ∼1 GPa to study its metastability [21–28]. Dynamic compression techniques are often used to access nonequilibrium conditions and explore kinetic behavior, which play a vital role in the phase transitions of many materials [29–31] including water [21–28, 32].

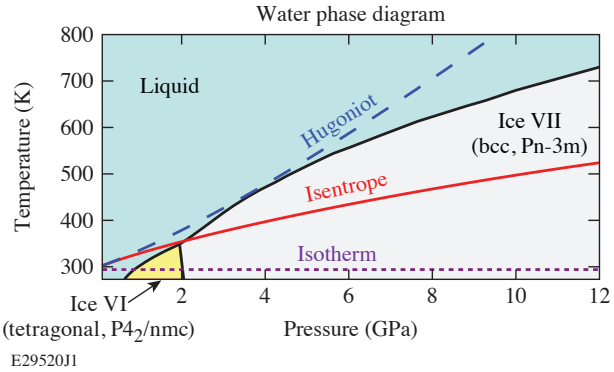

FIG. 1. Phase diagram of water relevant to our experiments. Ordinary water ice, ice Ih (hexagonal, $P6_3/mmc$), lies off the lower left corner and the ice VII-ice X (bcc, $Pn\text{-}\bar{3}m$) transition lies to the right at ∼40 to 80 GPa [12]. The equilibrium phase boundaries are from Ref. [10] and the principal Hugoniot, isentrope, and isotherm are from Ref. [13].

The metastability of liquid water transforming into ice VII has been the focus of many experimental [21, 23–28, 33] and theoretical [13, 34, 35] studies. Dolan *et al.* [23], Bastea *et al.* [33], and Nissen *et al.* [26] used velocimetry to investigate freezing when water was compressed quasi-isentropically (ramp compression) using pulsed-power drivers at rates of ∼0.1 GPa/ns. They found that water remained liquid in a metastable state beyond the liquid–ice VII equilibrium phase boundary [2.2 GPa on the principal isentrope (Fig. 1) [13]] until finally crystallizing homogeneously into ice VII at ∼6 to 7 GPa as indicated by a stress release signature or transient opacity. Hydrodynamics simulations of the Dolan *et al.* experiments using a kinetics model based on steady-state classical nucleation theory (CNT) confirmed the homogeneous nature of the nucleation and provided a detailed picture of the stress release signature [34, 36]. Using this CNT-based model for the solidification kinetics, Belof *et al.* predict that ramp-compressed liquid water has a metastability limit, above which the phase transition occurs no matter the compression rate, closer to 11 GPa [37]. This new theorized limit helps motivate experimental studies at even higher compression rates. Laser-driven experiments by Gleason *et al.* [27] compressed water $\gtrsim$10× more rapidly than Dolan *et al.* and measured the ice VII crystal structure after heterogeneous nucleation using *in-situ* x-ray diffraction. While these were the first dynamic-compression experiments to probe the

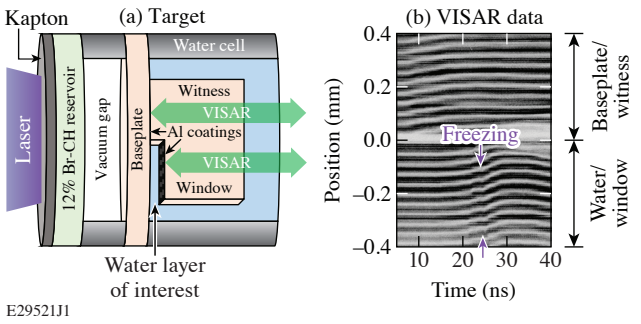

FIG. 2. (a) Target schematic and (b) VISAR image from experiment 29419 showing motion of the upper baseplate/witness interface and lower water/window interface.

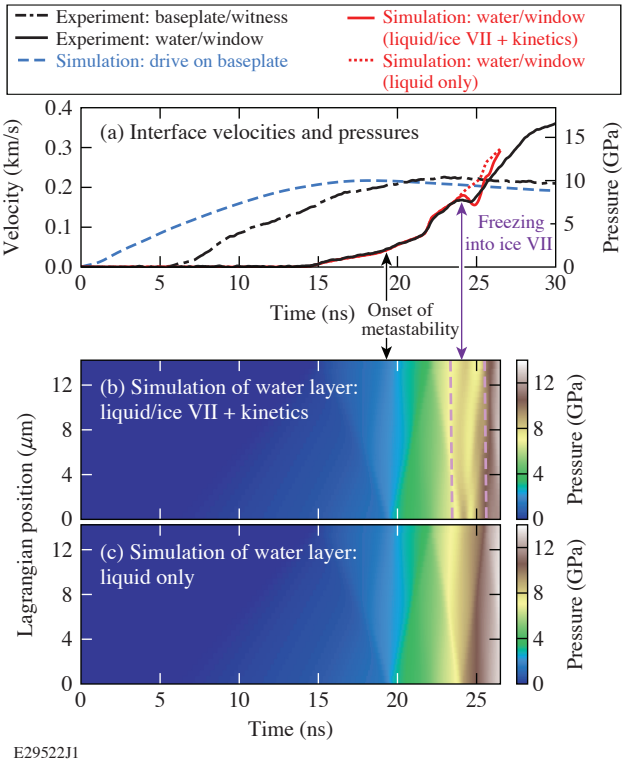

FIG. 3. Results from experiment 29419 and its simulations. Initial motion of the baseplate front surface (deduced from simulations of the witness side of the target) defines time 0. (a) Interface velocities and corresponding pressures (applicable to all curves). Lagrangian position versus time diagram of the pressure (colorbar) inside the water layer from the simulation using (b) the multiphase liquid+ice VII equation of state (EOS) and classical nucleation theory (CNT) based kinetics model and (c) only the liquid EOS (no phase transitions). Lagrangian position 0 and 14 correspond to the baseplate and window interface positions, respectively. The vertical dashed lines in (b) mark the onset and completion of freezing (same as Fig. 5)

ice's structure in real time, confirming that ice VII is indeed the nucleated phase in these high-pressure, ramp-compression experiments, they did not investigate the upper limit of the liquid's metastability [27].

We report on laser-driven experiments investigating the metastability of liquid water and the pressure at which it freezes into ice VII under ramp compression at rates up to 2.8 GPa/ns. We find that the metastability limit of liquid water on the principal isentrope is at least ∼8 GPa, ∼11% higher than the liquid–ice VII freezing pressure at ∼20× lower compression rates. We complement our experiments with simulations that provide further evidence that CNT using separate solid and liquid temperatures [36] can be used to predict phase-transition kinetics even at these extreme compression rates.

In this study, we ramp compress water to a peak pressure of ∼15 GPa over ∼15 ns on the OMEGA [38] and OMEGA EP [39] Laser Systems. A shockless ramp-compression wave is generated using a reservoir unloading technique [40–42]. Laser beams having a square-top pulse shape irradiate the polyimide (Kapton) ablator of the target shown in Fig. 2(a), launching a shock wave through the 12%-Br CH solid reservoir. The reservoir subsequently releases as a plasma plume across the vacuum gap, piling up on the front surface of the water cell, which ramp compresses the remainder of the target [40–42]. The target design for the ablator, reservoir, and vacuum gap (materials, thicknesses, Br dopant level) were chosen based on those of Refs. [40–42] to better predict the ramp compression profiles, timing, and possible preheat effects.

The water cell, filled with deionized 18 Mohm water, is an 850-μm-thick stainless-steel cylindrical cell sealed with a sapphire (36 to 152-μm-thick) or aluminum (30-μm-thick) baseplate at the front and an antireflective-coated sapphire window at the rear. A 7 to 33-μm water layer is created using a diving-board configuration as shown in Fig. 2(a). The sapphire or α-quartz block adhered to the baseplate acts as a "witness" to record shot-to-shot variations in the ramp-compression drive. The "window," sapphire or α-quartz (both z-cut crystals), encases the thin water layer. The pressures considered here are below the elastic limits of ∼20 GPa for sapphire [43, 44] and at least ∼10 GPa for α-quartz [44–46]. We do not expect phase transitions in the windows at these pressures [31, 47–53] (see Supplemental Material [54]). The window and witness are coated with ∼0.2 μm of aluminum on the laser drive side to provide a reflective surface for velocity measurements. Velocities of the water/window and baseplate/witness interfaces are measured through the rear of the target using a line-imaging velocity interferometer system for any reflector (VISAR) [55] [Fig. 2(b)] and known indices of refraction for sapphire [56] and α-quartz [57]. Interface velocity [u (km/s)] is converted to pressure [P (GPa)] using $P = 44.2u + 4.7u^2$ for sapphire [43] and $P = 16.74u + 3.31u^2 + 1.49u^3$ for α-quartz [44, 57]. In-

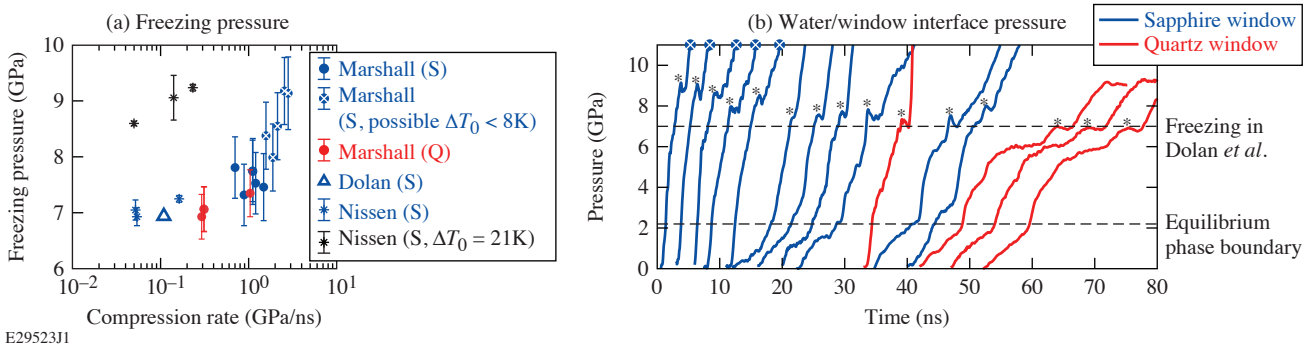

FIG. 4. (a) Liquid–ice VII freezing pressure versus compression rate (defined in the text) and (b) water/window interface pressure histories from our experiments, ordered by decreasing compression rate and shifted in time for clarity. In the legend of (a), S and Q denote sapphire and α-quartz windows, respectively, and ΔT_0 is the initial temperature increase above the principal isentrope, either known by controlled preheating of the sample (Nissen *et al.* [26]) or estimated for a possible initial shock that is indistinguishable from the steep ramp (this work). In (b), asterisks mark the pressure relaxation interpreted as freezing. The plateau several nanoseconds before freezing in the three right-most profiles using α-quartz windows is confirmed, using hydrocode simulations, to result from wave interactions arising from the ∼150-μm-thick baseplate. The plotted values from Nissen *et al.* [26] were taken directly from their publication (rates calculated over 5 to 11 GPa).

dividual target components and experimental configurations are given in the Supplemental Material [54].

A pressure relaxation on the window of the water layer, corresponding to a dip in the water/window interface velocity [e.g., near 24 ns in Figs. 2(b) and 3(a)], is observed despite the continuously increasing pressure drive. We interpret this drop in interface pressure as resulting from the volume collapse of the thin water layer when it freezes into the denser ice-VII phase; ice VII is ∼5% more dense than liquid water at 7 GPa on the principal isentrope [13].

By varying the laser energy, water and baseplate thicknesses, and materials (lower impedance α-quartz windows compared to sapphire lead to shallower pressure profiles), we investigate the metastability of liquid water when compressed at rates spanning 0.29 to 2.8 GPa/ns. We find that the measured liquid–ice VII freezing pressure (P_{freeze}) increases with compression rate [Fig. 4(a)], where P_{freeze} is the maximum pressure just before the dip denoting freezing and the compression rate, $(P_{\text{freeze}} - 2.2\ \text{GPa})/(t_{\text{freeze}} - t_{2.2\ \text{GPa}})$, is calculated from the onset of metastability to freezing, where t is the time at which the water/window interface reaches the corresponding pressures. P_{freeze} is calculated from the weighted average of the corresponding velocities at freezing from the two VISAR legs. Tabulated results and uncertainties are in the Supplemental Material [54].

The highest-measured liquid–ice VII freezing pressure from ambient conditions is at least 7.8±0.6 GPa but could be as high as 9.2±0.6 GPa, where additional heating of < 8 K above the principal isentrope during the loading cannot be ruled out (discussed below) [Fig. 4(a)]. These results indicate that liquid water's metastability limit is at least ∼11% higher in pressure than suggested by previous experiments at lower loading rates [23, 26, 33]. The water/window interface pressure histories for each experiment are shown in Fig. 4(b). Freezing occurs near 7 GPa when liquid water is compressed at ∼0.2 GPa/ns, which overlaps with previous experiments on water ramped from room temperature [23, 26] [Fig. 4(a)]. Our results agree with those of Dolan *et al.* [23] and Nissen *et al.* [26] despite all three works using different experimental drivers, baseplate materials (sapphire and copper), and window materials (Al-coated α-quartz, Al-coated sapphire, and uncoated sapphire). This agreement suggests that homogeneous nucleation in the bulk water layer is likely dominant as opposed to heterogeneous nucleation at the different interfaces or at impurity sites in the bulk. Ice VII is expected to nucleate homogeneously when the water in contact with sapphire (Al-coated or uncoated) [23–25, 28] and Al-coated silicas [28, 33] but heterogeneously (at lower compression rates) when the water is in direct contact with uncoated silicas [24, 25, 28].

In ultrafast ramp-compression experiments like these, the compression rate, material surrounding the water, and initial temperature all affect the phase-transition pressure. Nissen *et al.* [26] show that varying the initial temperature impacts the liquid–ice VII freezing pressure [Fig. 4(a)]; isentropes starting at higher temperatures cross the melt curve at higher pressures [26]. We examined the possibility of unintentional heating of the water by the laser-based compression source or the ramp wave steepening into a shock ramp. Our results agree with the initially room-temperature results of Nissen *et al.* [26] at 0.2 to 0.3 GPa/ns [Fig. 4(a)], suggesting that our water samples were not systematically preheated. It is unlikely that preheat from the laser ablation plasma is more significant at the higher compression rates because the laser intensities for shots with P_{freeze} of 9.2 GPa and 6.9 GPa differ by only ∼6%. Additionally, simulations

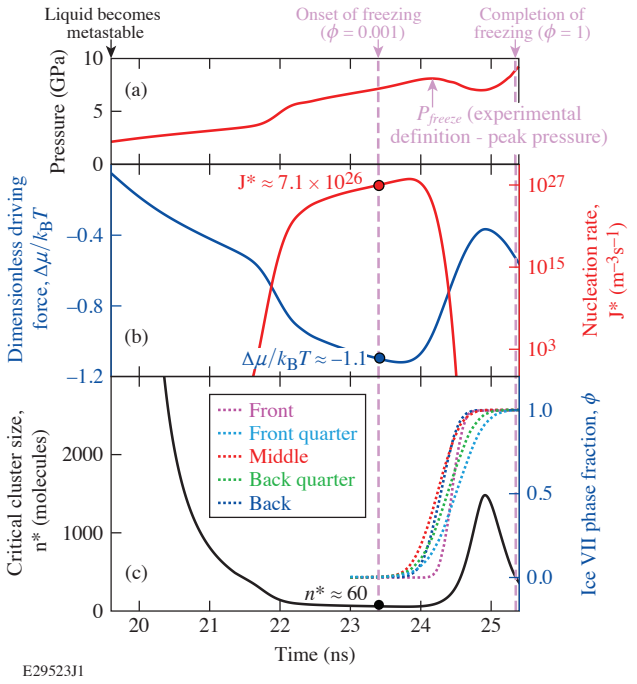

FIG. 5. Calculated observables from the simulation of experiment 29419 including the multiphase water EOS and CNT-based kinetics model [same as Figs. 3(a) and 3(b)]. (a) Water/window interface pressure [same red curve as Fig. 3(a)], (b) dimensionless driving force and nucleation rate, and (c) critical cluster size and ice VII phase fraction (dotted curves) at various locations from the baseplate (front) side to the window (back) side of the water layer.

using the radiation-hydrodynamics code *LASNEX* [58] suggest negligible preheat for similar targets and conditions [40, 54]. However, we cannot rule out formation of a small initial shock for the five experiments with the highest freezing pressures and steepest initial ramps at the water/window interface (white crosses in Fig. 4). These shots have ∼15-μm-thicker water layers [54], providing more opportunity for the ramp wave to steepen into a shock that would increase the entropy and temperature. Indeed, post-shot simulations of experiment 88458 (highest compression rate) using the *ARES* hydrodynamics code [59, 60] suggest that the thicker water layer causes initial wave steepening that raises the temperature by ∼7 K above the principal isentrope [54], which could partially account for the high ∼9 GPa freezing pressure [26]. The 100-mm-thick VISAR etalons needed for sufficient velocity precision have a ∼0.5 ns time delay. Because the VISAR effectively smears out velocity discontinuities over the time delay [61], we cannot distinguish a pure ramp from a ∼2 GPa shock-ramp at the sapphire window for shots 88458, 88459, and 90079 (highest compression rates). Heating from this potential ∼2 GPa reshock at the window and corresponding ∼1 GPa initial shock in the water would raise the temperature by ∼6-8 K above the principal isentrope [13, 54]. These results, like those from multi-shock experiments [23], are still valuable probes of the metastability limit even if there is some heating above the principal isentrope [34]. Using similar reasoning, we estimate ∼3-4 K of extra possible heating for shots 88460 and 90076 and negligible heating for the remaining shots, which all have lower compression rates and thinner water layers. See the Supplemental Material for more details [54].

Post-shot simulations of experiment 29419 were done using the *ARES* hydrodynamics code [59, 60] coupled to the *SAMSA* kinetics code [62], which uses the same CNT-based kinetics model from Ref. [36] that replicated the Dolan *et al.* [23] experimental observations. This CNT-based model uses separate solid and liquid temperatures, a small refinement to the interfacial free energy described in Ref. [36], and an initial temperature of 293 K. The experimentally measured baseplate/witness interface velocity was temporally smoothed, converted to pressure [43], and used as the time-dependent source (the "drive") on the baseplate/water/window portion of the target in the simulations [Fig. 3(a)]. Two simulations were performed. One simulation allowed freezing by using a multiphase liquid–ice VII EOS [13] and the CNT-based kinetics model [36]. The results are shown in Fig. 5 and Figs. 3(a) and 3(b) noted by "liquid/ice VII + kinetics." In this simulation, freezing initiates at ∼23.5 ns near the middle of the water layer and is completed after ∼2 ns, seen by the rise in ice VII phase fraction in Fig. 5(c) and the corresponding pressure dip in Fig. 3(b). The pressure dip at the water/window interface at 24 ns and 7.5 GPa that we observe in our experiment and attribute to freezing is also seen in the simulation in Fig. 3(a). The second simulation considered the null case (no phase transition) by using the liquid EOS only [noted by "liquid only" in Figs. 3(a) and 3(c)]. There is no pressure relaxation in this simulation at ∼24 ns in Fig. 3(a), reinforcing our interpretation that the experimentally observed dip is due to freezing and not unexpected wave reverberations in the target. Additional simulations [63] and details are in the Supplemental Material [54].

The simulations track a number of kinetic quantities to examine the underlying mechanisms governing freezing, all of which suggest that these experiments achieve a more deeply undercooled state ($\Delta T \approx 155$ K) than the previous Z-machine ramp-compression experiments on water (Dolan *et al.* [23]). The nucleation rate (J^*), number of molecules in a critical sized cluster (n^*), the dimensionless driving force ($\Delta\mu/k_BT$), and ice VII phase fraction (ϕ) are shown in Fig. 5, where $\Delta\mu = \mu_{solid} - \mu_{liquid}$ is the chemical potential difference between the solid ice VII and liquid state, k_B is the Boltzmann constant, and T is the temperature. Note that these quantities are calculated observables from simulations and are not directly determined by fitting to the experimental pressure profiles. Higher compression rates mean that the restor-

ing forces that drive the system back toward equilibrium have less time to act, and so intuitively, we expect the water to be overdriven to a more deeply undercooled state with increasing compression rate. Indeed, we find that the dimensionless driving force at the onset of freezing ($|\Delta\mu/k_{\mathrm{B}}T| \approx 1.1$), which reflects the extent of undercooling, is 10% larger than that of the Dolan *et al.* Z experiment [23, 36]. As a result, the nucleation rate is ∼1,000× larger in this work, and the critical-cluster size required for the successful nucleation and eventual macroscopic growth of ice VII is smaller [$n^* \approx 60$ molecules at the onset of freezing ($\phi = 0.1\%$), as opposed to $n^* \approx 75$ molecules for the Z experiment].

The metastability limit (where $\Delta G^* \approx k_{\mathrm{B}}T$ and ΔG is the nucleation energy barrier) along the principal (liquid) isentrope has been previously predicted, through application of nucleation theory, to reside near 11 GPa and nucleate with a critical cluster of around 52 molecules [37]. The experimental results presented here appear to support the theoretically predicted metastability limit for liquid water, although we suggest future studies at higher compression rates (carefully controlled to avoid formation of shocks) to further test this prediction.

In summary, we find that the metastability limit of liquid water on the principal isentrope is at least 8 GPa and that the liquid–ice VII freezing pressure increases with compression rate. The experiments reported here are at the frontier of experimental ultrafast science. It is remarkable that recent theoretical and numerical advances provide a detailed understanding of the observed phenomena, while relying on the fundamentally simple picture of homogeneous nucleation using CNT. This could have implications for our general understanding of phase transformations at extreme conditions.

We thank C. Davis, J. Fooks, R. Posadas, E. Folsom, and J. Emig for target fabrication and water cell development, the operations staff at the Omega Laser Facility, and J. R. Rygg and G. W. Collins for the helpful discussions. VISAR data were analyzed using LLNL's AnalyzeVisar code.

This work was performed under the auspices of the U.S. Department of Energy by Lawrence Livermore National Laboratory under Contract No. DE-AC52-07NA27344. This material is based upon work supported by the Department of Energy National Nuclear Security Administration under Award Number DE-NA0003856, the University of Rochester, and the New York State Energy Research and Development Authority. The support of DOE does not constitute an endorsement by DOE of the views expressed in this paper.

* michelle.marshall@rochester.edu

[1] M. Millot, S. Hamel, J. R. Rygg, P. M. Celliers, G. W. Collins, F. Coppari, D. E. Fratanduono, R. Jeanloz, D. C. Swift, and J. H. Eggert, Experimental evidence for superionic water ice using shock compression, Nat. Phys. **14**, 297 (2018).

[2] M. Millot, F. Coppari, J. R. Rygg, A. Correa Barrios, S. Hamel, D. C. Swift, and J. H. Eggert, Nanosecond X-ray diffraction of shock-compressed superionic water ice, Nature **569**, 251 (2019).

[3] T. Bartels-Rausch, V. Bergeron, J. H. E. Cartwright, R. Escribano, J. L. Finney, H. Grothe, P. J. Gutiérrez, J. Haapala, W. F. Kuhs, J. B. C. Pettersson, *et al.*, Ice structures, patterns, and processes: A view across the icefields, Rev. Mod. Phys. **84**, 885 (2012).

[4] G. Malenkov, Liquid water and ices: understanding the structure and physical properties, J. Phys.: Condens. Matter **21**, 283101 (2009).

[5] R. Yamane, K. Komatsu, J. Gouchi, Y. Uwatoko, S. Machida, T. Hattori, H. Ito, and H. Kagi, Experimental evidence for the existence of a second partially-ordered phase of ice VI, Nat. Commun. **12**, 1129 (2021).

[6] T. M. Gasser, A. V. Thoeny, A. D. Fortes, and T. Loerting, Structural characterization of ice XIX as the second polymorph related to ice VI, Nat. Commun. **12**, 1128 (2021).

[7] L. del Rosso, M. Celli, F. Grazzi, M. Catti, T. C. Hansen, A. D. Fortes, and L. Ulivi, Cubic ice Ic without stacking defects obtained from ice XVII, Nat. Mater. **19**, 663 (2020).

[8] K. Komatsu, S. Machida, F. Noritake, T. Hattori, A. Sano-Furukawa, R. Yamane, K. Yamashita, and H. Kagi, Ice Ic without stacking disorder by evacuating hydrogen from hydrogen hydrate, Nat. Commun. **11**, 464 (2020).

[9] L. Bezacier, B. Journaux, J.-P. Perrillat, H. Cardon, M. Hanfland, and I. Daniel, Equations of state of ice VI and ice VII at high pressure and high temperature, J. Chem. Phys. **141**, 104505 (2014).

[10] C. W. F. T. Pistorius, E. Rapoport, and J. B. Clark, Phase Diagrams of H_2O and D_2O at High Pressures, J. Chem. Phys. **48**, 5509 (1968).

[11] O. Tschauner, S. Huang, E. Greenberg, V. B. Prakapenka, C. Ma, G. R. Rossman, A. H. Shen, D. Zhang, M. Newville, A. Lanzirotti, and others., Ice-VII inclusions in diamonds: Evidence for aqueous fluid in Earth's deep mantle, Science **359**, 1136 (2018).

[12] P. Loubeyre, R. LeToullec, E. Wolanin, M. Hanfland, and

D. Hausermann, Modulated phases and proton centring in ice observed by X-ray diffraction up to 170 GPa, Nature **397**, 503 (1999).
[13] P. C. Myint, L. X. Benedict, and J. L. Belof, Free energy models for ice VII and liquid water derived from pressure, entropy, and heat capacity relations, J. Chem. Phys. **147**, 084505 (2017).
[14] G. Pallares, M. El Mekki Azouzi, M. A. González, J. L. Aragones, J. L. F. Abascal, C. Valeriani, and F. Caupin, Anomalies in bulk supercooled water at negative pressure, Proc. Natl. Acad. Sci. **111**, 7936 (2014).
[15] K. Amann-Winkel, R. Böhmer, F. Fujara, C. Gainaru, B. Geil, and T. Loerting, Colloquium: Water's controversial glass transitions, Rev. Mod. Phys. **88**, 011002 (2016).
[16] N. J. Hestand and J. L. Skinner, Perspective: Crossing the Widom line in no mans land: Experiments, simulations, and the location of the liquid-liquid critical point in supercooled water, J. Chem. Phys. **149**, 140901 (2018).
[17] P. Gallo, K. Amann-Winkel, C. A. Angell, M. A. Anisimov, F. Caupin, C. Chakravarty, E. Lascaris, T. Loerting, A. Z. Panagiotopoulos, J. Russo, *et al.*, Water: A tale of two liquids, Chem. Rev. **116**, 7463 (2016).
[18] J. A. Sellberg, C. Huang, T. A. McQueen, N. D. Loh, H. Laksmono, D. Schlesinger, R. G. Sierra, D. Nordlund, C. Y. Hampton, D. Starodub, *et al.*, Ultrafast X-ray probing of water structure below the homogeneous ice nucleation temperature, Nature **510**, 381 (2014).
[19] K. H. Kim, K. Amann-Winkel, N. Giovambattista, A. Späh, F. Perakis, H. Pathak, M. L. Parada, C. Yang, D. Mariedahl, T. Eklund, *et al.*, Experimental observation of the liquid-liquid transition in bulk supercooled water under pressure, Science **370**, 978 (2020).
[20] P. G. Debenedetti, F. Sciortino, and G. H. Zerze, Second critical point in two realistic models of water, Science **369**, 289 (2020).
[21] G. W. Lee, W. J. Evans, and C.-S. Yoo, Crystallization of water in a dynamic diamond-anvil cell: Evidence for ice VII-like local order in supercompressed water, Phys. Rev. B **74**, 134112 (2006).
[22] C. Lin, J. S. Smith, X. Liu, J. S. Tse, and W. Yang, Venture into Water's No Man's Land: Structural Transformations of Solid $\mathbf{H_2O}$ under Rapid Compression and Decompression, Phys. Rev. Lett. **121**, 225703 (2018).
[23] D. H. Dolan, M. D. Knudson, C. A. Hall, and C. Deeney, A metastable limit for compressed liquid water, Nat. Phys. **3**, 339 (2007).
[24] D. H. Dolan and Y. M. Gupta, Nanosecond freezing of water under multiple shock wave compression: Optical transmission and imaging measurements, J. Chem. Phys. **121**, 9050 (2004).
[25] D. H. Dolan, J. N. Johnson, and Y. M. Gupta, Nanosecond freezing of water under multiple shock wave compression: Continuum modeling and wave profile measurements, J. Chem. Phys. **123**, 064702 (2005).
[26] E. J. Nissen and D. H. Dolan, Temperature and rate effects in ramp-wave compression freezing of liquid water, J. Appl. Phys. **126**, 015903 (2019).
[27] A. E. Gleason, C. A. Bolme, E. Galtier, H. J. Lee, E. Granados, D. H. Dolan, C. T. Seagle, T. Ao, S. Ali, A. Lazicki, *et al.*, Compression freezing kinetics of water to ice vii, Phys. Rev. Lett. **119**, 025701 (2017).
[28] S. J. P. Stafford, D. J. Chapman, S. N. Bland, and D. E. Eakins, Observations on the nucleation of ice vii in compressed water, AIP Conf. Proc. **1793**, 130005 (2017).
[29] R. F. Smith, J. H. Eggert, D. C. Swift, J. Wang, T. S. Duffy, D. G. Braun, R. E. Rudd, D. B. Reisman, J.-P. Davis, M. D. Knudson, *et al.*, Time-dependence of the alpha to epsilon phase transformation in iron, J. Appl. Phys. **114**, 223507 (2013).
[30] R. F. Smith, J. H. Eggert, M. D. Saculla, A. F. Jankowski, M. Bastea, D. G. Hicks, and G. W. Collins, Ultrafast Dynamic Compression Technique to Study the Kinetics of Phase Transformations in Bismuth, Phys. Rev. Lett. **101**, 065701 (2008).
[31] S. J. Tracy, S. J. Turneaure, and T. S. Duffy, Structural response of α-quartz under plate-impact shock compression, Sci. Adv. **6**, eabb3913 (2020).
[32] Y.-J. Kim, Y.-H. Lee, S. Lee, H. Nada, and G. W. Lee, Shock growth of ice crystal near equilibrium melting pressure under dynamic compression, PNAS **116**, 8679 (2019).
[33] M. Bastea, S. Bastea, J. E. Reaugh, and D. B. Reisman, Freezing kinetics in overcompressed water, Phys. Rev. B **75**, 172104 (2007).
[34] P. C. Myint, A. A. Chernov, B. Sadigh, L. X. Benedict, B. M. Hall, S. Hamel, and J. L. Belof, Nanosecond freezing of water at high pressures: Nucleation and growth near the metastability limit, Phys. Rev. Lett. **121**, 155701 (2018).
[35] P. C. Myint and J. L. Belof, Rapid freezing of water under dynamic compression, J. Phys.: Condens. Matter **30**, 233002 (2018).
[36] D. M. Sterbentz, P. C. Myint, J.-P. Delplanque, and J. L. Belof, Numerical modeling of solid-cluster evolution applied to the nanosecond solidification of water near the metastable limit, J. Chem. Phys. **151**, 164501 (2019).
[37] J. L. Belof, L. X. Benedict, A. A. Chernov, S. Hamel, B. M. Hall, P. C. Myint, T. Oppelstrup, B. Sadigh, A. Samanta, D. M. Sterbentz, *et al.*, *Metastability and Kinetics of Solidification*, presented at the Research at High Pressure Gordon Research Conference, Holderness, NH, 15–20 July 2018.
[38] T. R. Boehly, D. L. Brown, R. S. Craxton, R. L. Keck, J. P. Knauer, J. H. Kelly, T. J. Kessler, S. A. Kumpan, S. J. Loucks, S. A. Letzring, *et al.*, Initial performance results of the OMEGA laser system, Opt. Commun. **133**, 495 (1997).
[39] D. D. Meyerhofer, J. Bromage, C. Dorrer, J. H. Kelly, B. E. Kruschwitz, S. J. Loucks, R. L. McCrory, S. F. B. Morse, J. F. Myatt, P. M. Nilson, *et al.*, Performance of and initial results from the OMEGA EP Laser System, J. Phys.: Conf. Ser. **244**, 032010 (2010).
[40] J. Edwards, K. T. Lorenz, B. A. Remington, S. Pollaine, J. Colvin, D. Braun, B. F. Lasinski, D. Reisman, J. M. McNaney, J. A. Greenough, *et al.*, Laser-Driven Plasma Loader for Shockless Compression and Acceleration of Samples in the Solid State, Phys. Rev. Lett. **92**, 075002 (2004).
[41] R. F. Smith, S. M. Pollaine, S. J. Moon, K. T. Lorenz, P. M. Celliers, J. H. Eggert, H.-S. Park, and G. W. Collins, High planarity x-ray drive for ultrafast shockless-compression experiments, Phys. Plasmas **14**, 057105 (2007).
[42] K. T. Lorenz, M. J. Edwards, A. F. Jankowski, S. M. Pollaine, R. F. Smith, and B. A. Remington, High pressure, quasi-isentropic compression experiments on the Omega laser, High Energy Density Phys. **2**, 113 (2006).
[43] O. V. Fatyanov, R. L. Webb, and Y. M. Gupta, Opti-

cal transmission through inelastically deformed shocked sapphire: stress and crystal orientation effects, J. Appl. Phys. **97**, 123529 (2005).

[44] B. M. LaLone, *Effect of Loading Rate and Peak Stress on the Elastic Limit of Dynamically Compressed Brittle Single Crystals*, Ph.D. Thesis, Washington State University (2011).

[45] X. Li, Y. Yu, Y. Li, L. Zhang, and J. Weng, Window corrections of z-cut quartz at 1550 nm under elastic, uniaxial compression up to 10 GPa, J. Appl. Phys. **109**, 103518 (2011).

[46] J. Wang, Z. Mao, F. Jiang, and T. S. Duffy, Elasticity of single-crystal quartz to 10GPa, Phys. Chem. Minerals **42**, 203 (2015).

[47] K. T. Thomson, R. M. Wentzcovitch, and M. S. T. Bukowinski, Polymorphs of Alumina Predicted by First Principles: Putting Pressure on the Ruby Pressure Scale, Science **274**, 1880 (1996).

[48] W. D. Reinhart, L. C. Chhabildas, and T. J. Vogler, Investigating phase transitions and strength in single-crystal sapphire using shockreshock loading techniques, Int. J. Impact Eng. **33**, 655 (2006).

[49] T. Mashimo, K. Tsumoto, K. Nakamura, Y. Noguchi, K. Fukuoka, and Y. Syono, High-pressure phase transformation of corundum (α-Al_2O_3) observed under shock compression, Geophys. Res. Lett. **27**, 2021 (2000).

[50] J. Hama and K. Suito, The evidence for the occurrence of two successive transitions in Al_2O_3 from the analysis of Hugoniot data, High Temp. High Press. **34**, 323 (2002).

[51] K. J. Kingma, R. J. Hemley, H.-K. Mao, and D. R. Veblen, New high-pressure transformation in α-quartz, Phys. Rev. Lett. **70**, 3927 (1993).

[52] R. J. Hemley, A. P. Jephcoat, H. K. Mao, L. C. Ming, and M. H. Manghnani, Pressure-induced amorphization of crystalline silica, Nature **334**, 52 (1988).

[53] J. Haines, J. M. Léger, F. Gorelli, and M. Hanfland, Crystalline Post-Quartz Phase in Silica at High Pressure, Phys. Rev. Lett. **87**, 155503 (2001).

[54] See Supplemental Material at [...] for tabulated results and for further details on the experimental configuration and simulations.

[55] P. M. Celliers, D. K. Bradley, G. W. Collins, D. G. Hicks, T. R. Boehly, and W. J. Armstrong, Line-imaging velocimeter for shock diagnostics at the OMEGA laser facility, Rev. Sci. Instrum. **75**, 4916 (2004).

[56] S. C. Jones, M. C. Robinson, and Y. M. Gupta, Ordinary refractive index of sapphire in uniaxial tension and compression along the c axis, J. Appl. Phys. **93**, 1023 (2003).

[57] S. C. Jones and Y. M. Gupta, Refractive index and elastic properties of z-cut quartz shocked to 60 kbar, J. Appl. Phys. **88**, 5671 (2000).

[58] G. B. Zimmerman and W. L. Kruer, Numerical simulation of laser-initiated fusion, Comments Plasma Phys. Control. Fusion **2**, 51 (1975).

[59] R. M. Darlington, T. L. McAbee, and G. Rodrigue, A study of ALE simulations of RayleighTaylor instability, Comp. Phys. Commun. **135**, 58 (2001).

[60] V. A. Dobrev, T. V. Kolev, and R. N. Rieben, High-order curvilinear finite element methods for Lagrangian hydrodynamics, SIAM J. Sci. Comput. **34**, B606 (2012).

[61] D. H. Dolan, Sandia National Laboratories Report No. SAND2006-1950 (2006).

[62] P. C. Myint, B. Sadigh, L. X. Benedict, D. M. Sterbentz, B. M. Hall, and J. L. Belof, Coupling solidification kinetics with phase-behavior computations in hydrodynamic simulations of high-pressure, dynamic-compression processes, AIP Adv. **10**, 125111 (2020).

[63] D. M. Sterbentz, J. R. Gambino, P. C. Myint, J.-P. Delplanque, H. K. Springer, M. C. Marshall, and J. L. Belof, Drive-pressure optimization in ramp-wave compression experiments through differential evolution, J. Appl. Phys. **128**, 195903 (2020).